PHYSICAL REVIEW B **92**, 201406(R) (2015)

Nonequilibrium spin texture within a thin layer below the surface of current-carrying topological insulator Bi_2Se_3: A first-principles quantum transport study

Po-Hao Chang,[1] Troels Markussen,[2] Søren Smidstrup,[2] Kurt Stokbro,[2] and Branislav K. Nikolić[1,*]
[1]*Department of Physics and Astronomy, University of Delaware, Newark, Delaware 19716-2570, USA*
[2]*QuantumWise A/S, Fruebjergvej 3, Box 4, DK-2100 Copenhagen, Denmark*
(Received 27 May 2015; revised manuscript received 29 July 2015; published 10 November 2015)

We predict that unpolarized charge current injected into a ballistic thin film of prototypical topological insulator (TI) Bi_2Se_3 will generate a *noncollinear spin texture* $\mathbf{S}(\mathbf{r})$ on its surface. Furthermore, the nonequilibrium spin texture will extend into an $\simeq$2-nm-thick layer below the TI surfaces due to penetration of evanescent wave functions from the metallic surfaces into the bulk of TI. Averaging $\mathbf{S}(\mathbf{r})$ over a few angstroms along the longitudinal direction defined by the current flow reveals a large component pointing in the transverse direction. In addition, we find an order of magnitude smaller out-of-plane component when the direction of injected current with respect to Bi and Se atoms probes the largest hexagonal warping of the Dirac-cone dispersion on the TI surface. Our analysis is based on an extension of the nonequilibrium Green's functions combined with density functional theory (NEGF+DFT) to situations involving noncollinear spins and spin-orbit coupling. We also demonstrate how DFT calculations with a properly optimized local orbital basis set can precisely match putatively more accurate calculations with a plane-wave basis set for the supercell of Bi_2Se_3.

DOI: 10.1103/PhysRevB.92.201406 PACS number(s): 72.25.Dc, 75.70.Tj, 71.15.Mb, 72.10.Bg

The newly discovered three-dimensional topological insulator (3D TI) materials possess a usual band gap in the bulk while also hosting metallic surfaces. The low-energy quasiparticles on these surfaces behave as massless Dirac fermions whose spins are locked to their momenta due to strong spin-orbit coupling (SOC) [1]. Such spin-momentum locking is viewed as a resource for spintronic applications [2]. For example, very recent experiments [3] have demonstrated magnetization dynamics of a single ferromagnetic metallic (FM) overlayer deposited on the surface of 3D TIs due to current-induced SO torques. Another recent experiment [4] has detected spin-to-charge conversion [5,6] when precessing magnetization of the FM overlayer pumps pure spin current into the metallic surface of 3D TIs.

The microscopic mechanism behind these phenomena can be traced to the so-called Edelstein effect (EE), originally predicted [7] for a *diffusive* two-dimensional electron gas (2DEG) with the Rashba SOC [8] and observed much later experimentally [9]. In the EE in 2DEG, longitudinal unpolarized charge current flowing along the x axis drives a homogeneous nonequilibrium spin density $\mathbf{S} = (0, S_y, 0)$ pointing in the transverse direction. The diffusive metallic surface of TIs also exhibits EE where a current-driven spin density $\mathbf{S}$ is substantially enhanced [2] (by a factor $\hbar v_F/\alpha_R \gg 1$, with v_F being the Fermi velocity in TI and α_R is the strength [8] of the Rashba SOC in 2DEG). Such enhancement can be explained by the spin-momentum locking along the single Fermi circle [1], formed in k space at the intersection of the Dirac cone energy-momentum dispersion and the Fermi energy plane, in contrast to spin-momentum locking along the two circles [8] in the case of Rashba 2DEG which counter the effect of each other. This has motivated recent experiments [10] probing $\mathbf{S}$ directly in three-terminal geometry where nonmagnetic electrodes inject unpolarized charge current into a TI, while a third FM contact deposited in the middle of the top surface of the TI film detects a voltage signal when a nonzero $\mathbf{S}$ is induced. These setups quantify the projection of $\mathbf{S}$ onto the magnetization of the third FM contact.

However, this picture of EE on the surface of TI is based on simplistic model Hamiltonians [2,3]. Here we employ a first-principles quantum transport approach to analyze microscopic details, over $\lesssim$1 Å length scale, of current-driven $\mathbf{S}(\mathbf{r})$ in the two-terminal *ballistic* thin film geometry hosting realistic TI material, as illustrated in Fig. 1. We choose Bi_2Se_3 as the prototypical TI material—with its single Dirac cone in the surface band structure, relatively large bulk band gap, and Dirac point (DP) inside the gap—on which many recent experiments probing EE directly [10] or indirectly [3,4] have been performed. The central region of the device in Fig. 1, which has length $L_x = 21.5$ Å along the x axis and infinite width along the y axis, is attached to two semi-infinite electrodes made of the same material. The electrodes are assumed to terminate at infinity into macroscopic Fermi liquid reservoirs where electrons are thermalized to acquire electrochemical potential μ_L in the left reservoir and μ_R in the right one. The Hamiltonian of the central region and the electrodes is obtained from the noncollinear density functional theory (ncDFT), implemented by us in the ATK package [11], using optimized pseudoatomic localized basis functions [12] and SOC introduced via the total-angular-momentum-dependent pseudopotentials [13]. The transport properties of the system in Fig. 1 are computed using the nonequilibrium Green's function (NEGF) formalism [14], so that our approach represents an extension of the widely used NEGF+DFT framework [15] to transport problems involving noncollinear spins and SOC.

In the simplest picture—based on effective Hamiltonian $\hat{H}_{\rm TI} = v_F(\hat{\boldsymbol{\sigma}} \times \hat{\mathbf{p}}) \cdot \mathbf{e}_z$ ($\hat{\boldsymbol{\sigma}}$ is the vector of the Pauli matrices, $\hat{\mathbf{p}}$ is the momentum operator, and $\mathbf{e}_z$ is the unit vector along the z axis in Fig. 1) describing massless Dirac electrons on the metallic surfaces of TIs—the spin and momentum of electronic eigenstates are orthogonal to each other along the single Fermi circle. This generates net homogeneous $\mathbf{S} = (0, S_y, 0)$ after an applied electric field E_x shifts the Fermi circle [2,3,16]

*bnikolic@udel.edu

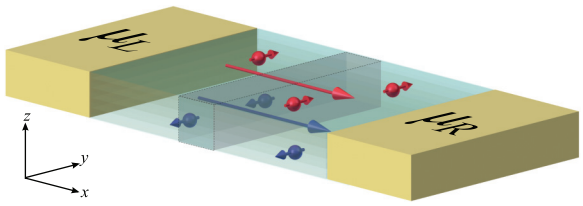

FIG. 1. (Color online) Schematic view of a two-terminal setup where a thin film of Bi_2Se_3 is attached to two macroscopic reservoirs biased by the electrochemical potential difference $eV_b = \mu_L - \mu_R$. The *clean* Bi_2Se_3 film is infinite along the x axis (i.e., the direction of transport) and the y axis, while its thickness along the z axis is chosen as five QLs. The shaded cell of length $d_x \simeq 5$ Å defines volume for averaging $\mathbf{S}(\mathbf{r})$ from Fig. 2, which is then plotted in Fig. 3 over the corresponding cross section of thin film within the yz plane.

along the momentum parallel to E_x. Such manifestation of EE persists in ballistic samples as well [17,18] where there is no electric field within the TI but instead one applies bias voltage $eV_b = \mu_L - \mu_R$ to inject a current into the TI, as illustrated in Fig. 1. The relations $S_y \propto E_x$ or $S_y \propto V_b$ describing EE in the diffusive or ballistic transport regimes, respectively, are allowed only in nonequilibrium since in equilibrium $\mathbf{S}$ changes sign under time reversal, and therefore has to vanish (assuming absence of magnetic field).

This simplistic picture can be contrasted with our principal results in Figs. 2 and 3. When a small (ensuring linear-response transport regime) V_b is applied between the reservoirs in Fig. 1, the unpolarized charge current injected into Bi_2Se_3 thin film generates a nonequilibrium $\mathbf{S}(\mathbf{r})$ whose complex *noncollinear* texture within three planes selected in Fig. 2(a) is plotted in Figs. 2(b) and 2(c). For the visualization we use a real-space grid for $\mathbf{r}$ whose spacing is $\simeq 0.4$ Å. Furthermore, Figs. 2 and 3 demonstrate that nonequilibrium spin texture $\mathbf{S}(\mathbf{r})$ will appear not only on the TI surface, but also within an $\simeq 2$-nm-thick layer of its bulk just below the top and bottom surfaces. This feature is explained in Figs. 3(a) and 3(b) showing the spatial profile of the local density of states (LDOS) at the Fermi energy E_F over the cell depicted in Fig. 1. The nonzero LDOS and the corresponding $\mathbf{S}(\mathbf{r})$ in the bulk of the TI thin film stem from evanescent wave functions which originate from the top and bottom metallic surfaces and penetrate into the energy gap of the insulating bulk. The Bi_2Se_3 prototypical TI is a strongly anisotropic material composed of quintuple layers (QLs) of Bi and Se atoms, illustrated in Fig. 2(a), where one QL consists of three Se layers strongly bonded to two Bi layers in between. For Bi_2Se_3 film thinner than five QLs, the evanescent wave functions from the top and bottom metallic surface can overlap to create a minigap [19,20] at the DP. We select the thickness of Bi_2Se_3 to be five QLs along the z axis in Fig. 1, which ensures that the LDOS in Figs. 3(a) and 3(b) goes to zero on the plane halfway between the top and bottom surfaces of the TI thin film.

Upon averaging nonequilibrium $\mathbf{S}(\mathbf{r})$ over a $d_x \simeq 5$ Å long cell depicted in Fig. 1, we obtain spatial profiles in Figs. 3(c) and 3(d) which show that S_y is the largest component independently of the direction of incoming electrons. An order of magnitude smaller S_z component shown in Fig. 3(d) appears for electrons incoming along current direction 2 marked in panel (e). This is in accord with experiments in equilibrium where spin- and angle-resolved photoemission spectroscopy [21] finds the largest out-of-plane spin component along the corresponding direction in the 2D Brillouin zone (BZ). This is due to hexagonal warping of the Dirac cone surface band structure,

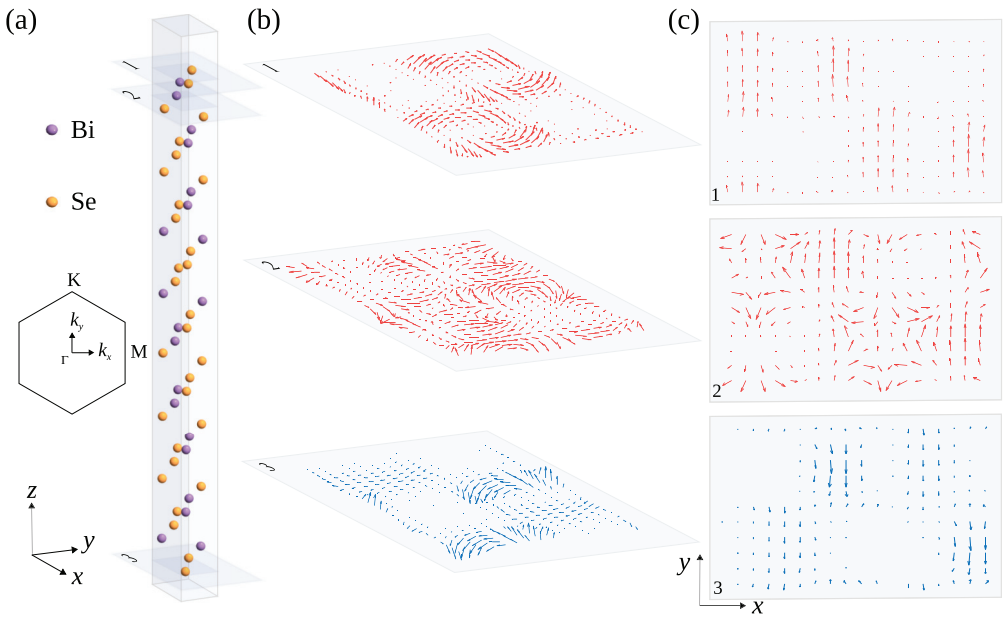

FIG. 2. (Color online) (a) The arrangement of Bi and Se atoms within a supercell of Bi_2Se_3 thin film of thickness five QLs. The inset in panel (a) shows BZ in the k_x-k_y plane at $k_z = 0$ with special k points Γ, M, and K marked. (b) The vector field of nonequilibrium $\mathbf{S}(\mathbf{r})$ within selected planes shown in (a), generated by injection of unpolarized charge current along the x axis (see also Fig. 1). The planes 1 and 3 correspond to the top and bottom metallic surfaces of Bi_2Se_3 thin film, while plane 2 resides in the bulk at a distance $d \approx 0.164$ nm away from plane 1. (c) The vector fields in (b) projected onto each of the selected planes in (a). The real space grid of $\mathbf{r}$ points in panels (b) and (c) has spacing $\simeq 0.4$ Å.

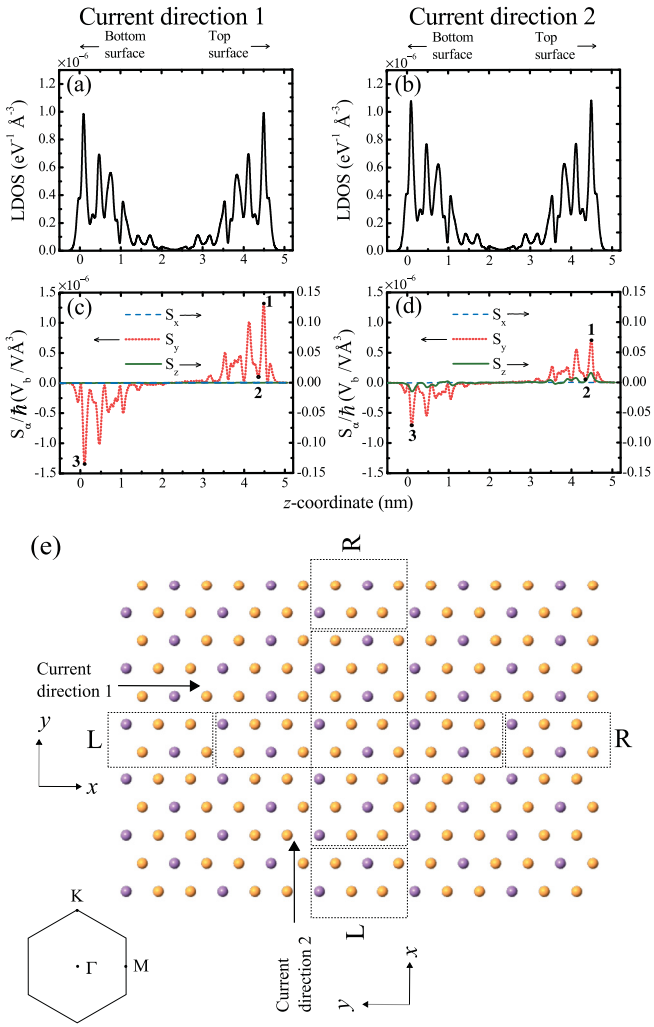

FIG. 3. (Color online) (a),(b) The spatial profile of LDOS at E_F over the cross section of the cell denoted in Fig. 1. (c),(d) The spatial profile of the components of $\mathbf{S}(\mathbf{r})$, obtained by averaging its texture plotted in Fig. 2, over the cell of Bi_2Se_3 thin film marked in Fig. 1. The direction of injected charge current for the results in panels (a) and (c), or the results in panels (b) and (d), is denoted in panel (e) relative to the orientation of the lattice of Bi and Se atoms. The bottom surface of Bi_2Se_3 is located at $z = 0$ nm, and the top TI surface is located at $z \approx 4.56$ nm. In panels (c) and (d) we also mark the positions of planes 1–3 from Fig. 2.

as confirmed by DFT calculations [19,22] finding that the equilibrium expectation value of spin in the eigenstates of Bi_2Se_3 surfaces tilts out of the 2D BZ. Thus, Fig. 3 offers a novel prescription for probing hexagonal warping via transport measurements where charge current is injected in different directions relative to the orientation of the lattice of Bi and Se atoms.

We now explain the technical details of our calculations. The extension of DFT to the case of spin-polarized systems is formally derived in terms of total electron density $n(\mathbf{r})$ and vector magnetization density $\mathbf{m}(\mathbf{r})$. In the collinear DFT, $\mathbf{m}(\mathbf{r})$ points in the same direction at all points in space, which is insufficient to study magnetic systems where the direction of the local magnetization is not constrained to a particular axis or systems governed by SOC. In ncDFT [23], the exchange-correlation (XC) functional $E_{\rm XC}[n(\mathbf{r}),\mathbf{m}(\mathbf{r})]$ depends on $\mathbf{m}(\mathbf{r})$

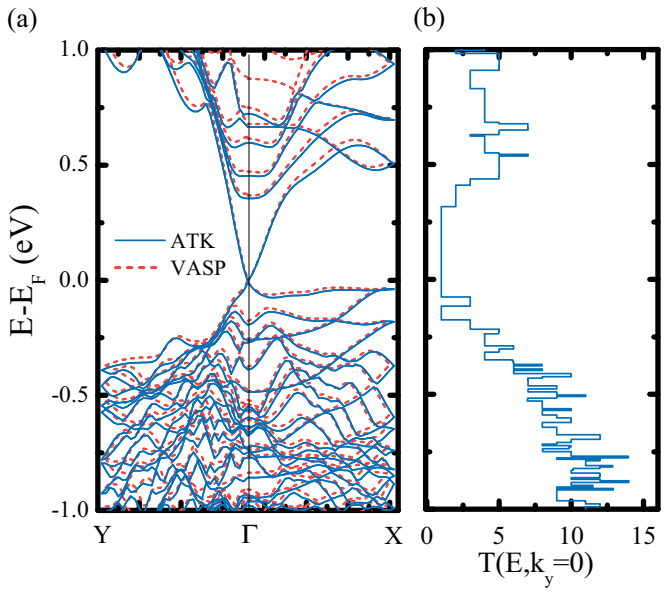

FIG. 4. (Color online) (a) The electronic band structure computed for a supercell of Bi_2Se_3 film shown in Fig. 2(a) using LCAO [12] ncDFT implemented in the ATK [11] package. This is compared with the electronic band structure obtained using PW ncDFT implemented in the VASP package [26]. (b) Zero-bias transmission function of Bi_2Se_3 thin film in the two-terminal geometry of Fig. 1, for electrons injected along the Γ-M direction ($k_y = 0$) in the inset of Fig. 2(a), computed using NEGF+ncDFT formalism implemented in the ATK package.

pointing in arbitrary directions. The local density approximation and most often employed version of generalized gradient approximation (GGA), implemented also by us in ATK [11], make additional approximations [23] that lead to the XC magnetic field $\mathbf{B}_{\rm XC}(\mathbf{r}) = \delta E_{\rm XC}[n(\mathbf{r}),\mathbf{m}(\mathbf{r})]/\delta\mathbf{m}(\mathbf{r})$ being parallel everywhere to $\mathbf{m}(\mathbf{r})$.

The single-particle spin-dependent Kohn-Sham (KS) Hamiltonian in ncDFT takes the form

$$\hat{H}_{\rm KS} = -\frac{\hbar^2\nabla^2}{2m} + V_{\rm H}(\mathbf{r}) + V_{\rm XC}(\mathbf{r}) + V_{\rm ext}(\mathbf{r}) - \boldsymbol{\sigma}\cdot\mathbf{B}_{\rm XC}(\mathbf{r}), \quad (1)$$

where $V_{\rm H}(\mathbf{r})$, $V_{\rm ext}(\mathbf{r})$, and $V_{\rm XC}(\mathbf{r}) = \delta E_{\rm XC}[n(\mathbf{r}),\mathbf{m}(\mathbf{r})]/\delta n(\mathbf{r})$ are the Hartree, external, and XC potential, respectively. Diagonalization of $\hat{H}_{\rm KS}$ proceeds by approximating the Hilbert space of all single-electron eigenfunctions with a finite set of basis functions. A popular basis set is plane waves (PWs), where varying only one parameter (the energy cutoff) allows one to improve the basis systematically. Linear combination of atomic orbitals (LCAO) basis sets require more tuning; however, they simplify the NEGF calculations [15] where one has to spatially separate the system into the central region and semi-infinite electrodes, as illustrated in Fig. 1.

Since the pioneering screening [24] of candidate TI materials via ncDFT calculations, their electronic band structure has most often been calculated [19,20] using PW ncDFT with electron-core interactions described via the projector augmented wave (PAW) method [25]. In Fig. 4(a) we demonstrate that such calculations, performed by the VASP package [26], can be accurately reproduced by pseudopotential-based LCAO ncDFT implemented in ATK [11]. The supercell considered in

both calculations is shown in Fig. 2(a), which includes five QLs terminated by Se atomic layer on both the top and bottom surface, as well as a 7.5-Å-thick vacuum layer above and below these Se atomic layers.

We note that previous attempts [22] to apply pseudopotential-based LCAO ncDFT to Bi_2Se_3 have yielded either poor accuracy of its electronic band structure [e.g., compare our Fig. 4(a) with Fig. 1 in Ref. [22]] or have required intricate fine tuning [27]. Therefore, we provide here a complete recipe for the proper usage of LCAO ncDFT to reproduce Fig. 4(a). In ATK calculations in Fig. 4(a), the electron-core interactions are described by norm-conserving pseudopotentials. The pseudopotentials are obtained by mapping the solution of the Dirac equation, which naturally includes SOC, [13] to nonrelativistic pseudopotential, $V_{\rm PS} = V_{\rm L} + V_{\rm NL}^{1/2} + V_{\rm NL}^{-1/2}$, with local contribution $V_{\rm L}$ and nonlocal contributions $V_{\rm NL}$ from the total angular momentum $j = l + 1/2$ and $j = l - 1/2$. The nonlocal terms are expanded in terms of SO projector functions, $V_{\rm NL}^{\pm 1/2} = \sum_{l,\xi,\alpha,\beta} \nu_{l\pm 1/2,\xi} P_{\alpha\beta}^{l\pm 1/2,\xi}$, where $\nu_{l\pm 1/2,\xi}$ are normalization constants and the indices α,β denote the possible spin orientations $(\uparrow,\downarrow)$. We use Perdew-Burke-Ernzerhof (PBE) parametrization of GGA for the XC functional and a LCAO basis set $\{\phi_i\}$ generated by the OPENMX package [12,28], which consists of $s2p2d1$ orbitals on Se atoms and $s2p2d2$ on Bi atoms. These pseudoatomic orbitals were generated by a confinement scheme [12] with the cutoff radius 7.0 and 8.0 a.u. for Se and Bi atoms, respectively. The energy mesh cutoff for the real-space grid is chosen as 75.0 hartree. In VASP calculations [26] in Fig. 4(a), the electron-core interactions are described by the PAW method [25], and we employ PBE GGA for the XC functional. The cutoff energy for the PW basis set is 350 eV. In both ATK and VASP calculations we employ $11 \times 11 \times 1$ k-point mesh within the Monkhorst-Pack scheme for the BZ integration.

The eigenstates $|\Psi_n\rangle$ of the KS Hamiltonian in Eq. (1) make it possible to construct the equilibrium density matrix $\boldsymbol{\rho}_{\rm eq} = \sum_n |\Psi_n\rangle\langle\Psi_n| f(E)$ for electrons at $\mu_L = \mu_R$ and temperature T described by the Fermi distribution function $f(E)$. The local electron and magnetization density, as the central variables of ncDFT, are obtained from $n(\mathbf{r}) = \langle\mathbf{r}|{\rm Tr}_{\rm spin}[\boldsymbol{\rho}_{\rm eq}]|\mathbf{r}\rangle$ and $\mathbf{m}(\mathbf{r}) = \langle\mathbf{r}|{\rm Tr}_{\rm spin}[\boldsymbol{\rho}_{\rm eq}\boldsymbol{\sigma}]|\mathbf{r}\rangle$, where the trace is taken over the spin Hilbert space.

In steady-state nonequilibrium due to dc current flowing between the left and right reservoirs in Fig. 1, we construct the nonequilibrium density matrix [29] $\boldsymbol{\rho}_{\rm neq}$ using NEGFs:

$$\boldsymbol{\rho}_{\rm neq} = \frac{1}{2\pi i}\int_{-\infty}^{+\infty} dE\, \mathbf{G}^{<}(E) - \boldsymbol{\rho}_{\rm eq}. \qquad (2)$$

This yields $\mathbf{S}(\mathbf{r}) = \frac{\hbar}{2}\langle\mathbf{r}|{\rm Tr}_{\rm spin}[\boldsymbol{\rho}_{\rm neq}\boldsymbol{\sigma}]|\mathbf{r}\rangle$ plotted in Figs. 2 and 3. The NEGF formalism [14] for steady-state transport operates with two central quantities—the retarded GF, $\mathbf{G}(E)$, and the lesser GF, $\mathbf{G}^{<}(E)$—which describe the density of available quantum states and how electrons occupy those states, respectively. In the absence of inelastic processes, these are given by $\mathbf{G} = [E\mathbf{O} - \mathbf{H}_{\rm KS} - \boldsymbol{\Sigma}_L - \boldsymbol{\Sigma}_R]$ and $\mathbf{G}^{<} = i\mathbf{G}[f_L\boldsymbol{\Gamma}_L + f_R\boldsymbol{\Gamma}_R]\mathbf{G}^{\dagger}$. Here the self-energies $\boldsymbol{\Sigma}_{L,R}$ are due to semi-infinite electrodes, $f_{L,R} = f(E - \mu_{L,R})$ and $\boldsymbol{\Gamma}_{L,R} = i(\boldsymbol{\Sigma}_{L,R} - \boldsymbol{\Sigma}_{L,R}^{\dagger})$ is the level broadening matrix. For the chosen LCAO basis set, the Hamiltonian matrix $\mathbf{H}_{\rm KS}$ is composed of elements $\langle\phi_i|\hat{H}_{\rm KS}|\phi_j\rangle$ and the overlap matrix $\mathbf{O}$ is composed of elements $\langle\phi_i|\phi_j\rangle$. In the linear-response transport regime considered here, Eq. (2) can be expanded [29] to first order in bias voltage V_b. Since $\mathbf{S}(\mathbf{r})$ is zero in equilibrium (because of the assumed absence of an external magnetic field), the linear-response density matrix can be simplified to [29] $\boldsymbol{\rho}_{\rm neq} = \frac{eV_b}{2\pi}\int_{-\infty}^{+\infty} dE\, \mathbf{G}\boldsymbol{\Gamma}_L\mathbf{G}^{\dagger}(-\frac{\partial f}{\partial E})$. Otherwise, the gauge-invariant form of $\boldsymbol{\rho}_{\rm neq}$ requires additional terms [29] to properly remove the equilibrium expectation value of a considered physical quantity.

The retarded GF also allows us to obtain the transmission function of the device in Fig. 1, $T(E,k_y) = {\rm Tr}[\boldsymbol{\Gamma}_R\mathbf{G}\boldsymbol{\Gamma}_L\mathbf{G}^{\dagger}]$, which depends on energy and transverse momentum k_y due to assumed periodicity in the y direction. The total transmission function $T(E)$ is obtained by integrating over k_y, which determines the linear-response conductance via the Landauer formula, $G = \frac{e^2}{h}\int dE\, T(E)(-\frac{\partial f}{\partial E})$. We confirm in Fig. 4(b) that $T(E,k_y = 0) = 2$ for E within the bulk gap shown in Fig. 4(a) because only one doubly degenerate helical conducting channel is open for transport in that energy range [30] for injected electrons with momentum along the Γ-M direction ($k_y = 0$).

In conclusion, using the NEGF+ncDFT framework implemented by us in the ATK package [11], we computed a nonequilibrium spin texture $\mathbf{S}(\mathbf{r})$ within a thin film of current-carrying Bi_2Se_3 TI material. The nonzero texture appears on the TI metallic top and bottom surfaces, as well as within bulk layers of thickness $\simeq 2.0$ nm below the surfaces that effectively dope the bulk by evanescent wave functions. The spin texture is noncollinear and complex on length scales $\lesssim 1$ Å. Upon averaging it over a few angstroms we find a simpler pattern (in accord with EE discussed using model Hamiltonians [2])—where either $\mathbf{S} = (0,S_y,0)$, or $\mathbf{S} = (0,S'_y,S'_z)$ with $S'_y/S'_z \gg 1$, depending on the direction of injected current with respect to orientation of the lattice of Bi and Se atoms. Such dependency offers a novel probe, via electronic transport measurements [10], of the hexagonal warping of the Dirac cone surface band structure. For the envisaged spintronic applications of TIs, it is essential to understand how $\mathbf{S}(\mathbf{r})$ changes due to finite bias voltage or self-consistent coupling [31] to magnetization of a ferromagnetic (metal or insulator) overlayer, which we relegate to future studies.

P.-H.C. and B.K.N. were supported by NSF Grant No. ECCS 1509094. The supercomputing time was provided by XSEDE, which is supported by NSF Grant No. ACI-1053575. QuantumWise acknowledges support from the Danish Innovation Fund Grant No. 79-2013-1: "Nano-scale design tools for the semiconductor industry."

[1] M. Z. Hasan and C. L. Kane, Rev. Mod. Phys. **82**, 3045 (2010); X.-L. Qi and S.-C. Zhang, *ibid.* **83**, 1057 (2011).

[2] D. Pesin and A. H. MacDonald, Nat. Mater. **11**, 409 (2012).

[3] A. R. Mellnik *et al.*, Nature (London) **511**, 449 (2014); Y. Fan *et al.*, Nat. Mater. **13**, 699 (2014).
[4] Y. Shiomi, K. Nomura, Y. Kajiwara, K. Eto, M. Novak, K. Segawa, Y. Ando, and E. Saitoh, Phys. Rev. Lett. **113**, 196601 (2014).
[5] F. Mahfouzi, N. Nagaosa, and B. K. Nikolić, Phys. Rev. B **90**, 115432 (2014).
[6] K. Shen, G. Vignale, and R. Raimondi, Phys. Rev. Lett. **112**, 096601 (2014).
[7] V. M. Edelstein, Solid State Comm. **73**, 233 (1990); A. G. Aronov and Y. B. Lyanda-Geller, JETP Lett. **50**, 431 (1989).
[8] R. Winkler, *Spin-Orbit Coupling Effects in Two-Dimensional Electron and Hole Systems* (Springer, Berlin, 2003).
[9] Y. K. Kato, R. C. Myers, A. C. Gossard, and D. D. Awschalom, Phys. Rev. Lett. **93**, 176601 (2004); A. Yu. Silov, P. A. Blajnov, J. H. Wolter, R. Hey, K. H. Ploog, and N. S. Averkiev, Appl. Phys. Lett. **85**, 5929 (2004); S. D. Ganichev, S. N. Danilov, P. Schneider, V. V. Bel'kov, L. E. Golub, W. Wegscheider, D. Weiss, and W. Prettl, J. Magn. Magn. Mater. **300**, 127 (2006).
[10] C. H. Li, O. M. J. van 't Erve, J. T. Robinson, Y. Liu, L. Li, and B. T. Jonker, Nat. Nanotechnol. **9**, 218 (2014); Y. Ando, T. Hamasaki, T. Kurokawa, K. Ichiba, F. Yang, M. Novak, S. Sasaki, K. Segawa, Y. Ando, and M. Shiraishi, Nano Lett. **14**, 6226 (2014); L. Liu, A. Richardella, I. Garate, Y. Zhu, N. Samarth, and C.-T. Chen, Phys. Rev. B **91**, 235437 (2015); J. Tian, I. Miotkowski, S. Hong, and Y. P. Chen, Sci. Rep. **5**, 14293 (2015).
[11] Atomistix ToolKit (ATK) 2014.2, http://www.quantumwise.com.
[12] T. Ozaki, Phys. Rev. B **67**, 155108 (2003); T. Ozaki and H. Kino, *ibid.* **69**, 195113 (2004).
[13] G. Theurich and N. A. Hill, Phys. Rev. B **64**, 073106 (2001).
[14] G. Stefanucci and R. van Leeuwen, *Nonequilibrium Many-Body Theory of Quantum Systems: A Modern Introduction* (Cambridge University Press, Cambridge, 2013).
[15] J. Taylor, H. Guo, and J. Wang, Phys. Rev. B **63**, 245407 (2001); M. Brandbyge, J. L. Mozos, P. Ordejon, J. Taylor, and K. Stokbro, *ibid.* **65**, 165401 (2002); D. A. Areshkin and B. K. Nikolić, *ibid.* **81**, 155450 (2010).
[16] T. Misawa, T. Yokoyama, and S. Murakami, Phys. Rev. B **84**, 165407 (2011).
[17] S. Modak, K. Sengupta, and D. Sen, Phys. Rev. B **86**, 205114 (2012).
[18] P.-H. Chang, F. Mahfouzi, N. Nagaosa, and B. K. Nikolić, Phys. Rev. B **89**, 195418 (2014).
[19] O. V. Yazyev, J. E. Moore, and S. G. Louie, Phys. Rev. Lett. **105**, 266806 (2010).
[20] K. Park, J. J. Heremans, V. W. Scarola, and D. Minic, Phys. Rev. Lett. **105**, 186801 (2010).
[21] Z.-H. Pan, E. Vescovo, A. V. Fedorov, D. Gardner, Y. S. Lee, S. Chu, G. D. Gu, and T. Valla, Phys. Rev. Lett. **106**, 257004 (2011); M. Nomura, S. Souma, A. Takayama, T. Sato, T. Takahashi, K. Eto, K. Segawa, and Y. Ando, Phys. Rev. B **89**, 045134 (2014).
[22] Y. Zhao, Y. Hu, L. Liu, Y. Zhu, and H. Guo, Nano Lett. **11**, 2088 (2011).
[23] K. Capelle, G. Vignale, and B. L. Györffy, Phys. Rev. Lett. **87**, 206403 (2001); F. G. Eich, S. Pittalis, and G. Vignale, Phys. Rev. B **88**, 245102 (2013).
[24] H. Zhang, C.-X. Liu, X.-L. Qi, X. Dai, Z. Fang, and S.-C. Zhang, Nat. Phys. **5**, 438 (2009).
[25] P. E. Blöchl, Phys. Rev. B **50**, 17953 (1994); G. Kresse and D. Joubert, *ibid.* **59**, 1758 (1999).
[26] G. Kresse and J. Hafner, Phys. Rev. B **47**, 558 (1993); G. Kresse and J. Furthmüller, *ibid.* **54**, 11169 (1996); Comput. Mater. Sci. **6**, 15 (1996).
[27] P. Rivero, V. M. Garcí-Suárez, D. Pereñiguez, K. Utt, Y. Yang, L. Bellaiche, K. Park, J. Ferrer, S. Barraza-Lopez, Comput. Mater. Sci. **98**, 372 (2015).
[28] See http://www.openmx-square.org/.
[29] F. Mahfouzi, N. Nagaosa, and B. K. Nikolić, Phys. Rev. Lett. **109**, 166602 (2012); F. Mahfouzi and B. K. Nikolić, SPIN **3**, 1330002 (2013).
[30] X.-F. Wang, Y. Hu, and H. Guo, Phys. Rev. B **85**, 241402 (2012); A. Narayan, I. Rungger, A. Droghetti, and S. Sanvito, *ibid.* **90**, 205431 (2014).
[31] Y. G. Semenov, X. Duan, and K. W. Kim, Phys. Rev. B **89**, 201405 (2014).